Acta Metallurgica Sinica (English Letters) (2022) 35:212–222
https://doi.org/10.1007/s40195-021-01283-5

Facile Preparation of NiO@graphene Nanocomposite with Superior Performances as Anode for Li-ion Batteries

Junke Ou[1,2] · Shugen Wu[3] · Lin Yang[4] · Hao Wang[5]

Received: 8 February 2021 / Revised: 26 April 2021 / Accepted: 1 June 2021 / Published online: 21 July 2021

Abstract
Transition metal oxides gain considerable research attentions as potential anode materials for lithium ion batteries, but their applications are hindered due to their poor electronic conductivity, weak cycle stability and drastic volume change. Here, a NiO@graphene composite with a unique 3D conductive network structure is prepared through a simple strategy. When applied as anode material for Li-ion batteries, at 50 mA g^{-1}, the NiO@graphene displays a high reversible capacity of 1366 mAh g^{-1} and a stable cyclability of 205 mAh g^{-1} after 500 cycles. Even at a high rate of 10 A g^{-1}, it displays a favorable reversible capacity of 711 mAh g^{-1}. Remarkably, when it recovers back to 0.05 A g^{-1}, a reversible capacity of 1741 mAh g^{-1} is achieved. Thus, the NiO@graphene composite with 3D structure shows good application prospects as an alternative anode for advanced lithium ion batteries.

Keywords Lithium ion batteries · 3D conductive network structure · NiO@graphene composite · Alternative

1 Introduction

Recently, Li-ion batteries (LIBs) have aroused great attentions and are considered as ubiquitous power sources for portable electronic equipment and electrical vehicles due to their long lifespan, superior energy density as well as absence of memory effects [1–5]. With increased market demand, the research and development for the anode materials with high performances are in urgent need [6–8]. However, the anode of commercial graphite with a low theoretical capacity of 372 mAh g^{-1} for LIBs cannot satisfy the increasing demand for large-scale energy storage applications [9]. Hence, it is necessary to develop superior anode materials with large capacity in future high power LIBs.

In recent years, it has been reported that transition metal oxides (TMOs, like NiO, CuO, SnO_2, Fe_3O_4, Co_3O_4, etc.) can be effectively served as anode electrodes for LIBs due to the larger theoretical capacities (over 500 mAh g^{-1}) and the excellent reaction potential with lithium ion [10, 11]. Remarkably, NiO is regarded as a promising candidate among TMOs for the favorable theoretical capacity (718 mAh g^{-1}), environmental friendliness, low price, natural abundance and safety [12–14]. Nevertheless, there are some inevitable weaknesses, such as poor conductivity and large volume changes in pure NiO anodes during the cycling process, which leads to the partial pulverization of electrode materials and the fast decline in capacity [15–17]. To overcome these challenges, a variety of nanostructured NiO anode materials, such as nanoparticle [18], nanorod [19], nanosheet [20] and nanotube [21], have been successfully synthesized, and all of them make an outstanding breakthrough in the electrochemical performances. Unfortunately, it may lead to the aggregation of materials and severe side reactions, which affects the cycling and rate performances [22, 23]. Moreover, carbonaceous matrixes with structural stability, flexibility, large surface area and high electrical conductivity play a crucial role in

Available online at http://link.springer.com/journal/40195.

✉ Junke Ou
ojk0001@163.com

1 Institute for Advanced Study, Chengdu University, Chengdu 610106, China

2 Material Corrosion and Protection Key Laboratory of Sichuan Province, Sichuan University of Science and Engineering, Zigong 643000, China

3 Zhanglan Honors College, Chengdu University, Chengdu 610106, China

4 School of Medicine, Chengdu University, Chengdu 610106, China

5 School of Mechanical Engineering, Chengdu University, Chengdu 610106, China

improving the electrochemical properties. It is reported that $La_{11.3}Mg_{6.0}Sm_{7.4}Ni_{61.0}Co_{7.2}Al_{7.1}$ showed an excellent high-rate discharge ability properties with a retention rate of 89.6% at a discharge current density of 1750 mA/g by the addition of graphene [24]. Wang et al. synthesized Si@SiO_x particles with a thin coated carbon layer, which provided a capacity of 1230 mA h g^{-1} after 100 cycles at 500 mA g^{-1} [25]. The discharge capacity loss over 200 cycles was only about 0.21% per cycle for P-milled Si/graphene nanocomposite [26]. Based on their desirable advantages, carbon can act as a special protective layer, which not only inhibits volume changes of NiO, but also prevents NiO aggregating [13, 27]. For example, after 100th cycle at 0.1 A g^{-1}, the NiO/C hollow microspheres display a large discharge capacity of 628 mAh g^{-1} [28]. Li et al. showed that the egg shell-yolk NiO/C porous composites still could give a steady capacity of 400 mAh g^{-1} at 800 mA g^{-1} [29]. NiO_x-carbon composite fibers also possessed a favorable capacity of 676 mAh g^{-1} at 500 mA g^{-1} after the 200th cycle [30].

Graphene, a two-dimensional (2D) net-like sheet structure composed of sp^2 carbon atoms arranged in a hexagonal honeycomb lattice, was found in 2004 [31]. Since then, numerous interests have been focused on graphene due to the desirable features in high specific surface area, good mechanical flexibility, preferable electronic conductivity, rapid electron transfer and pronounced chemical stability [32, 33]. For instance, the few-layer graphene can be obtained via plasma-assisted ball milling [34]. In comparison with other kinds of carbon, this few-layer graphene with extremely high conductivity exhibits fast electron transport highway, more reactive sites, forceful capability to accommodate volume expansion and superior contact with matrix, which is beneficial for the improvement in electrochemical properties [24, 35]. As a promising matrix material, graphene was always superior to other carbon-based metal oxides in terms of electrochemical performances [36]. Therefore, with the purpose of optimizing properties of anodes for LIBs, the research on the combination of NiO and graphene is of great significance.

Herein, in this study, we developed a NiO@graphene composite with a three-dimensional (3D) conductive network structure. It is worth nothing that such unique structure can enhance the material's conductivity and inhibit the structure change of NiO during discharge–charge cycles. Thus, the as-obtained NiO@graphene displays stable cyclic performance (205 mAh g^{-1} after 500 cycles at 0.05 A g^{-1}) and superior rate performance of 711 mAh g^{-1} even at an extreme high rate of 10 A g^{-1}.

2 Experimental

2.1 Fabrication of NiO@graphene Composite

NiO@graphene was prepared by a simple and facile strategy. Typically, 2.852 g nickel chloride hexahydrate ($NiCl_2{\cdot}6H_2O$) and 1.44 g urea were dissolved in 60 ml triple distilled water and magnetically stirred to get a homogeneous solution. Subsequently, the solution was placed into the autoclave and reacted at 90 °C for 12 h. After the final solution was cooled down, the as-obtained precursor was washed with triple distilled water and dried at 60 °C for 24 h in vacuum. Furthermore, the obtained precursor was pyrolyzed in air at 500 °C for 2 h. The as-prepared nickle oxide and 5 wt% graphene (obtained from Nanjing Xianfeng nanomaterial technology Co., Ltd) were mixed together in 10 ml ethanol and stirred magnetically for 30 min and finally dried at 40 °C overnight under vacuum.

2.2 Electrochemical Testing

The working electrode was fabricated by thoroughly blending 80 wt% active materials, 10 wt% acetylene black and 10 wt% polyvinylidene fluoride (PVDF) in N-methyl-2-pyrrolidone (NMP) and uniformly coated onto a copper foil. Afterward, the slurry was dried at 80 °C in vacuum. Coin-type batteries (CR2032) were made in an Ar-filled glove box (Dellix 750 s) by applying the Celgard-2400 film as the separator, Li foil as the counter electrode and 1 M $LiPF_6$ dissolved in ethylene carbonate (EC)/dimethyl carbonate (DMC)/ethyl-methyl carbonate ethylene (EMC) (1:1:1 by volume) with addition of 2% vinyl carbonate (VC) as the electrolyte. The electrochemical property investigations were conducted on NEWARE system (CT-3008) between 0.01 V and 3 V at room temperature.

2.3 Material Characterization

The X-ray diffraction (XRD) was conducted with Cu-*K*α radiation using a TD-3500 X-ray powder diffractometer (Tongda, China). Thermal gravimetric analysis (TGA) was carried out on a thermo gravimetric analyzer (Q500, USA) with a ramping rate of 5 °C min^{-1} from room temperature to 500 °C in air. Raman spectra were determined by a confocal Lab RAM HR800 spectrometer. The surface morphology of the materials was performed on a scanning electron microscopy (SEM, Hitachi S4800). The transmission electron microscopy (TEM, FEI Tecnai G2 20, Hillsboro, OR, USA) was used to investigate the microstructures. X-ray photoelectron spectroscopy (XPS)

was analyzed applying a Kratos XSAM 800 spectrometer (Manchester, UK).

3 Results and Discussion

From the XRD pattern of the as-synthesized precursor in Fig. 1a, the characteristic peaks centered at 34.7° and 59.8° are well assigned to the (101) and (110) of the α-$Ni(OH)_2$ phase, respectively [37], indicating that the precursor prepared in the hydrothermal process was nickel hydroxide. Figure 1b exhibits the thermo gravimetric (TG) analysis of the $Ni(OH)_2$ from room temperature to 500 °C with a ramping rate of 5 °C/min in air. We can clearly see that the amount of NiO in $Ni(OH)_2$ is about 60.5 wt%, which is assigned to the mass loss of water. According to the result of TG, the nominal formula of the material is considered to be $Ni(OH)_2 \cdot 1.7H_2O$. The XRD patterns of pure NiO and NiO@graphene composite are presented in Fig. 1c. Two samples with diffraction peaks at the 2θ values of 37.4°, 43.4°, 62.9° and 75.7° could be well indexed to (111), (200), (220) and (311) crystal planes of cubic-phased NiO, respectively [38]. An additional low and small peak (2$\theta \approx 25.7°$) was found in pattern of the NiO@graphene, corresponding to the diffraction peak of the multilayer graphene sheets [39]. The Raman spectra of the as-prepared materials are displayed in Fig. 1d. There are two characteristic peaks at approximately 1359 and 1609 cm^{-1} for NiO@graphene composite, assigning to the D band and G band of graphene, manifesting NiO and graphene were well synthesized [40]. On the contrary, there are no D band and G band seen from NiO, which might be no carbon involved. All above results showed the combination of the NiO and graphene.

Figure 2a–c depicts the SEM images of $Ni(OH)_2$, NiO and NiO@graphene, respectively. The $Ni(OH)_2$ is made up of microparticles with a diameter of about 1–2 μm, and NiO particles show a similar morphology after the pyrolysis of the $Ni(OH)_2$ (Fig. 2a, b). Figure 2c shows that the NiO particles were embedded in the graphene sheets, which is conducive to the construction of the efficient electron transport

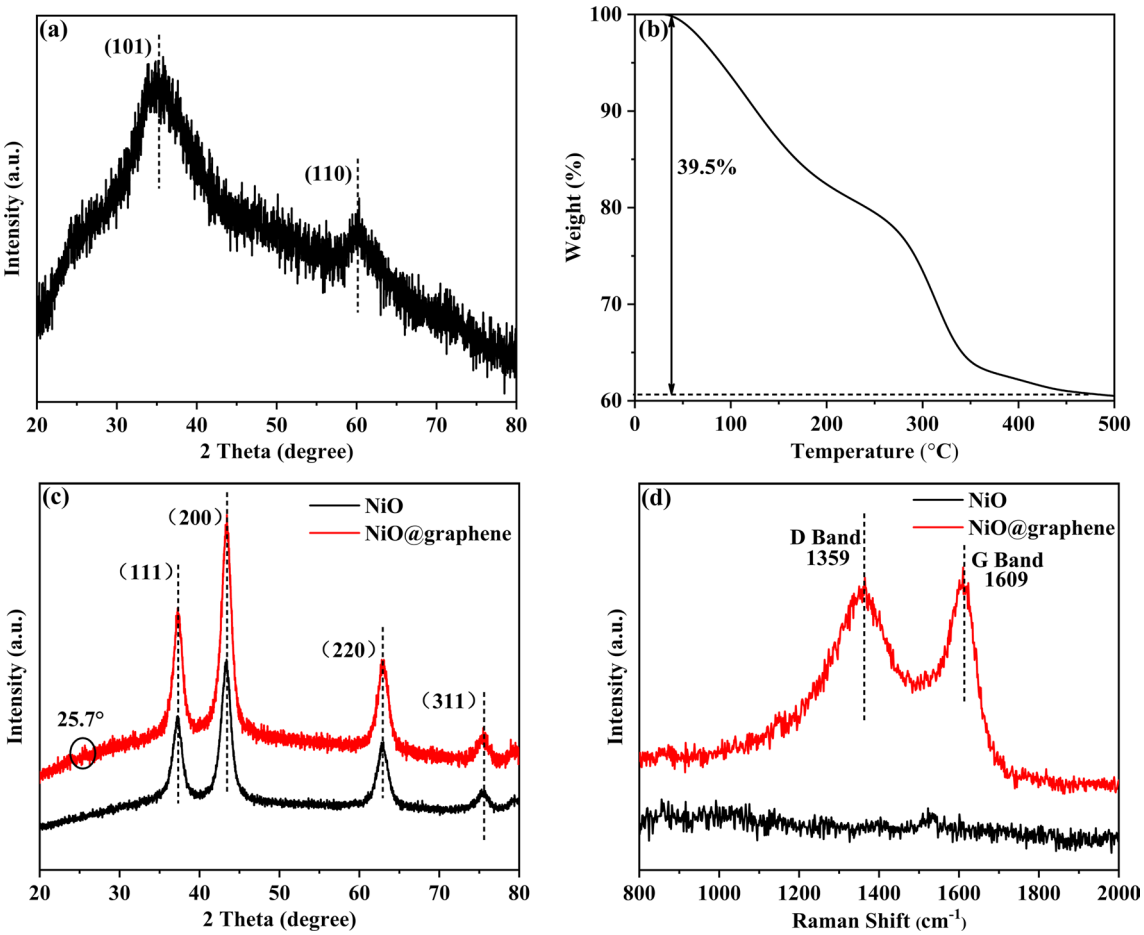

Fig. 1 XRD pattern of the precursor **a**, TGA curve of $Ni(OH)_2$ **b**, XRD patterns of NiO and NiO@graphene **c**, Raman spectra of NiO and NiO@graphene **d**

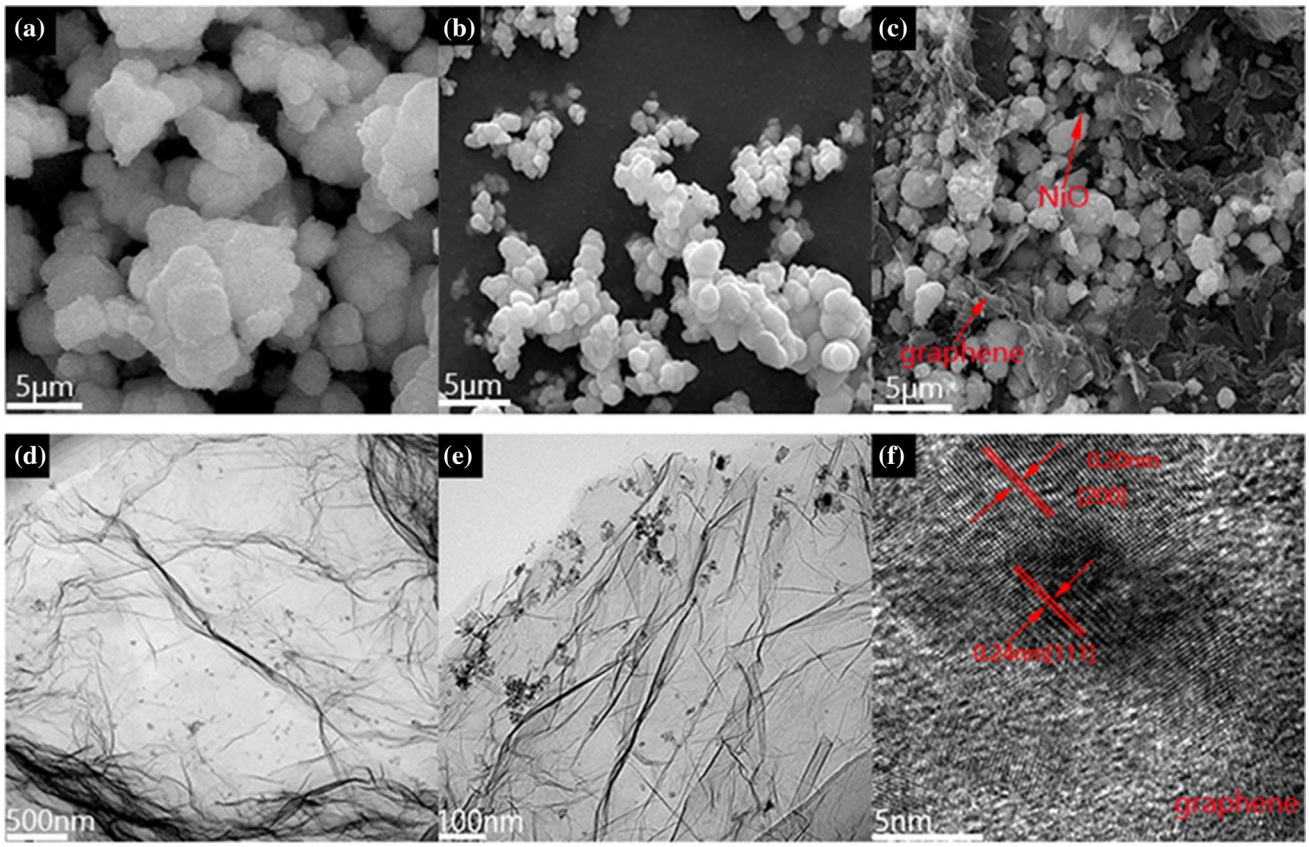

Fig. 2 SEM images of $Ni(OH)_2$ **a**, NiO **b**, NiO@graphene **c**, TEM images **d e**, HRTEM image **f** of NiO@graphene

channels. The morphology and microstructures of NiO@graphene can be further characterized by TEM. From the TEM images (Fig. 2d, e), some nanoparticles are attached to the surface of graphene layers, which indicates that the NiO and graphene were well combined. Meanwhile, these results are consistent with those of XRD and Raman. Figure 2f depicts the high-resolution TEM (HRTEM) image of the NiO@graphene; the core–shell structure is indicative of presence of graphene. Moreover, two obvious interplanar distances are around 0.20 nm and 0.24 nm, which is attributed to the (200) and (111) lattice plane of cubic-phase NiO [41].

The corresponding selected-area electron diffraction (SAED) patterns of NiO@graphene (Fig. S1), in which three Debye–Scherrer rings were clearly observed, can be attributed to (111), (200) and (220) crystal planes of the crystalline NiO phase [42].

XPS analysis (Fig. 3) is employed to further understand the surface chemical composition of NiO@graphene. Figure 3a reveals that NiO@graphene possesses the Ni, O and C. From Fig. 3b, two characteristic peaks are observed at 854.9 and 872.6 eV, which are designated to the Ni $2p_{3/2}$ and Ni$2p_{1/2}$, respectively [43]. The spin energy separation between two Ni $2p_{3/2}$ and Ni$2p_{1/2}$ is around 17.7 eV, revealing the oxidation state of Ni^{2+} [44]. Meanwhile, there are two peaks located at 861.1 and 878.8 eV, corresponding to the satellite peaks of Ni $2p_{3/2}$ and Ni$2p_{1/2,}$ respectively [45]. Three fitted peaks centered at 284.7, 285.9 and 288.6 eV are designated to C–C/C=C, C–O–C and O=C–O bonds in Fig. 3c, respectively [46]. Remarkably, the C–C/C=C peak displays the strongest intensity in all peaks, which can be beneficial for improving the electrical conductivity of NiO@graphene specimen [47]. Figure 3d shows three peaks at 529.6, 531.7 and 533.5 eV, which corresponds to the O atoms chemically bonded in Ni–O, Ni–OH and O–C=O, respectively [48]. The peak between carbon and oxygen indicates that there may be some interaction between graphene and the oxygen in NiO [45].

The cyclic voltammetry (CV) profiles of the NiO and NiO@graphene between 0.01 and 3 V at a scanning rate of 0.1 mV s^{-1} for the initial three cycles are exhibited in Fig. 4a–b. During the first cathodic cycles of NiO electrode, a sharp peak at about 0.45 V is observed, which could be derived from the formation of the solid electrolyte interface (SEI) layer and reduction of NiO to Ni via a conversion reaction ($NiO + 2Li^+ + 2e^- \rightarrow Ni + Li_2O$) [17, 21]. Then, this main cathodic peak is shifted to 0.97 V in the subsequent cycles, caused by intense structural modification [49].

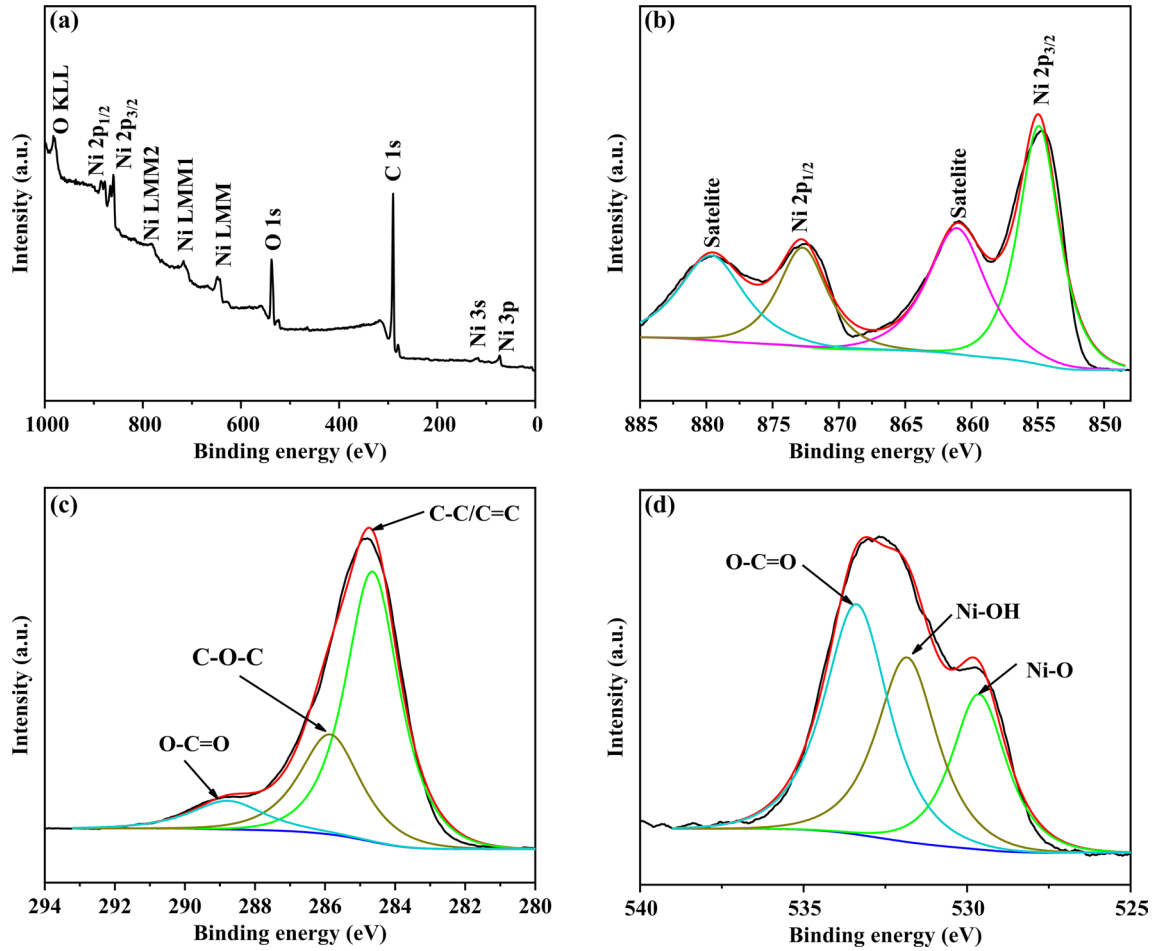

Fig. 3 XPS analysis of NiO@graphene composite: survey spectrum **a**, Ni 2*p* **b**, C 1 *s* **c**, O 1 *s* **d**

Meanwhile, two major peaks at about 1.45 V and 2.26 V are detected in anodic sweep, corresponding to partial decomposition of SEI layers and oxidation of Ni^0 to NiO ($Ni + Li_2O \rightarrow NiO + 2Li^+ + 2e^-$), respectively [50, 51]. As for NiO@graphene electrode, there is a different peak at about 0.47 V in the cathodic part of the first sweep, which also can be in agreement with formation of a SEI film and reduction of NiO to Ni, and Li_xC ($C + xLi^+ + xe^- \rightarrow Li_xC$) [15]. Besides, a main peak at 0.93 V is designated to the reduction of NiO [52]. The obvious different cathodic behavior can be derived from the addition of graphene with large specific surface area and the improvement in electronic conductivity of NiO@graphene composite [53]. Moreover, the SEI layers decomposition and the conversion of NiO to Ni^0 peaks are similar to that of NiO electrode in the anodic process [54, 55]. Figure 4c, d displays the charge and discharge potential curves of NiO and NiO@graphene at 50 mA g^{-1} after the 1st, 2nd, 5th, 10th, 20th and 30th cycles, respectively. The initial cycled charge and discharge capacities of the NiO are 800 mAh g^{-1} and 1104 mAh g^{-1}, respectively, and the initial Coulombic efficiency (ICE) is 72.5%. Compared with NiO, the ICE of NiO@graphene is 70.7%, led by the charge and discharge capacities of 860 mAh g^{-1} and 1217 mAh g^{-1}, respectively. Both the cells exhibit the high initial irreversible capacity loss at the initial cycle, which could be due to the SEI film [56]. The reason for the low ICE of NiO@graphene may be attributed to the graphene, which can cause a higher initial capacity loss [54, 57]. Besides, the reversible capacity of NiO drops to 856 mAh g^{-1} at the 30th cycle. Meanwhile, the reversible capacity of NiO@graphene has a growing trend, rising from 936 to 993 mAh g^{-1} (20th to 30th cycle), which is due to the activation of electrode materials and the formation/dissolution of a gel-like polymeric film during cycling process [42, 58]. From Fig. S2, the ICEs of NiO with 3 wt% and 8 wt% graphene are 66.6% and 63.1%, respectively. Clearly, it can be found that 8 wt% graphene has little effect on the reversible of NiO@graphene, which just contributes to the same reversible capacity of 840.5 mAh g^{-1} as pure NiO at the 5th cycle. NiO with 3 wt% graphene displays a desirable reversible capacity of 886 mAh g^{-1} at the 5th cycle. These results suggest that 3 wt% and 5 wt% graphene both can make an

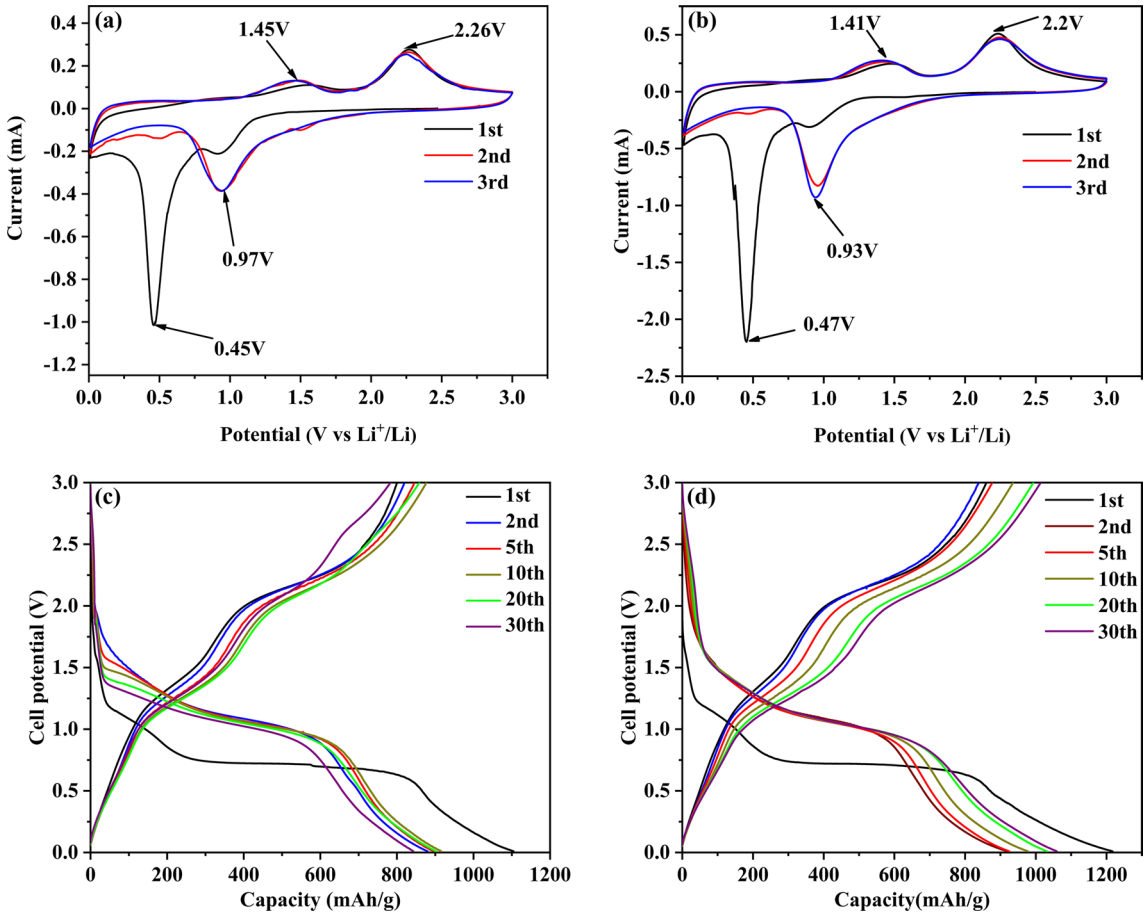

Fig. 4 CV profiles of NiO **a,** NiO@graphene **b** electrodes at a scanning rate of 0.1 mV s^{-1} ranging from 0.01 to 3.0 V. Discharge and charge curves of NiO **c,** NiO@graphene **d** materials at 0.05 A g^{-1}

improvement on the reversible capacity of NiO@graphene. Taking the ICE into consideration, however, adding 5 wt% graphene may be an appropriate choice for NiO.

To compare the rate capability and cycling property of two samples, both electrodes measured at different rates from 0.05 to 10 A g^{-1} are illustrated in Fig. 5a. As the current density was enhanced between 0.05 and 5 A g^{-1}, the NiO@graphene delivers superior reversible capacities of 1366, 1390, 1410, 1390, 1346, 1222 and 742 mAh g^{-1}. For NiO, the reversible capacities are 1028, 1109, 1074, 976, 818, 616, 381 mAh g^{-1} at the rates of 0.05, 0.1, 0.2, 0.5, 1, 2 and 5 A g^{-1}, respectively. Notably, for NiO@graphene, the reversible capacity can increase from 381 to 711 mAh g^{-1} even tested at an extreme large current density of 10 A g^{-1} (about 27 C, 1C = 372 mAh/g), which is much larger than that of NiO (about 200 mAh g^{-1}). When it comes back to 0.05 A g^{-1}, it accounts for the good reversibility and stability of the materials. Particularly, as to NiO@graphene, the reversible capacity can be increased to 1741 mAh g^{-1} as the current returns to 0.05 A g^{-1}, which is much larger than the capacity remaining after the first 5 cycles. These good results manifest that NiO@graphene electrode has more superior rate performance probably due to the conductive network structure of graphene and the improvement in the lithium ion diffusion capability. The cycling property of two materials was conducted at 0.05 A g^{-1} in Fig. 5b. It is evident that NiO displays continuous and dramatic capacity decay from the 40th cycle, only reserving a fairly low reversible capacity of 92 mAh g^{-1} after 500 cycles. In sharp contrast, NiO@graphene unfolds significantly improved cycling performance and its reversible capacity shows a steady upward trend during initial 70 cycles. It is especially noteworthy that the reversible capacity of NiO@graphene can reach up to 1560 mAh g^{-1} at the 70th cycle, corresponding to 143.3% capacity retention of the first cycle. This fascinating upward tendency may be derived from two aspects: (1) the inevitable formation of a gel-like polymer layer and the slight degradation of SEI film during the reduction process of NiO to Ni [29] and (2) graphene nanosheets that cannot only retard the structure expansion of NiO but also relieve the aggregation of active materials [1, 15]. Then, the NiO@graphene material also displays a decreased reversible capacity of

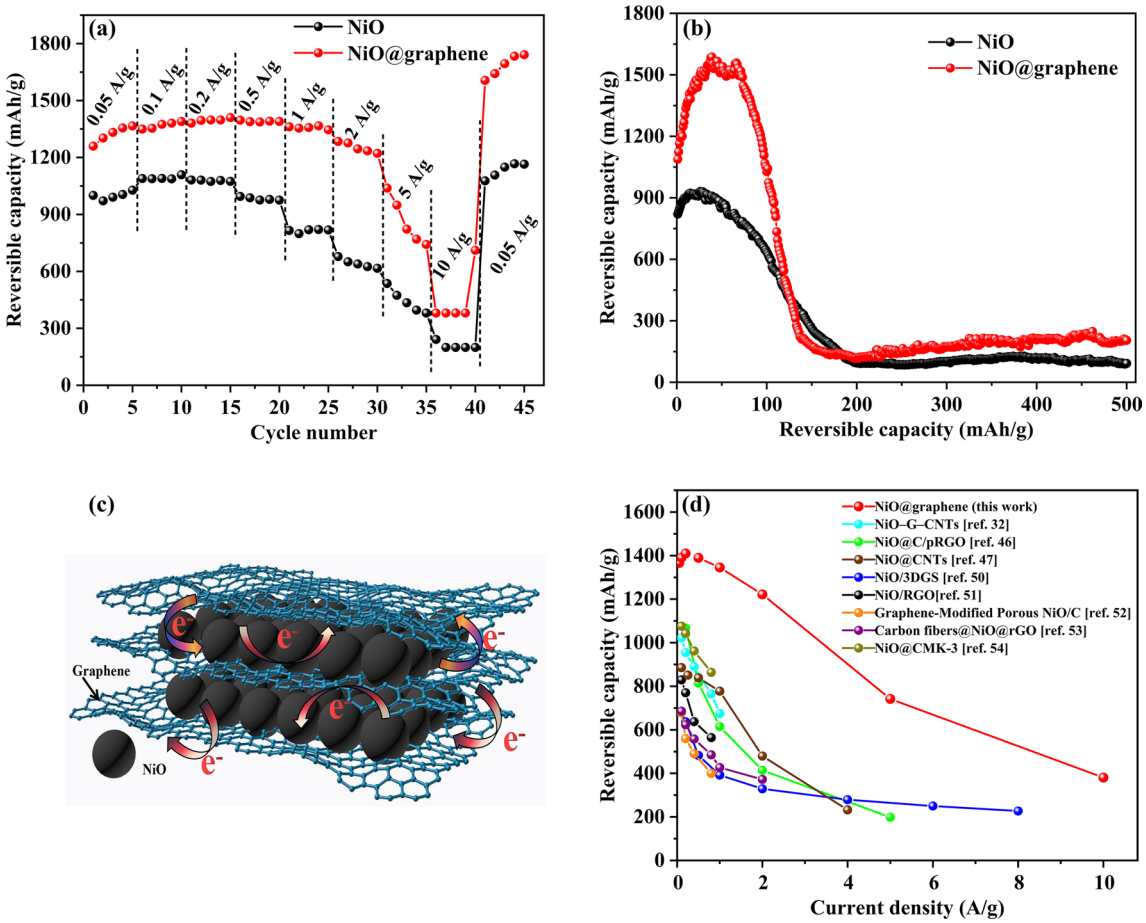

Fig. 5 Rate performance and cyclability curves for both NiO and NiO@graphene under various current densities from 0.05 to 10 A g^{-1} **a**, cycling property for two samples at 0.05 A g^{-1} for 500 cycles **b**, 3D structure of NiO@graphene **c**, comparison of the rate capability between NiO@graphene and other NiO/C composites anodes previously reported **d**

116 mAh g^{-1} at the 200th cycle, which may be ascribed to the formation of lithium dendrites and the destruction of part of the polymeric gel-like film [59]. After 500 cycles, the reversible capacity of NiO@graphene can still be stable at 205 mAh g^{-1}. To a certain extent, the 3D hierarchical structure of NiO@graphene can buffer the deformation of the NiO nanoparticles, thus resulting in a better cycling property than NiO. For further exploring the morphology and structural expansion during the Li^+ intercalation/deintercalation processes, the SEM analysis on the NiO and NiO@graphene electrodes before and after the 100th cycle is performed in Fig. S3. Both cells discharged to 0.01 V after 100 cycles were disassembled and then analyzed by SEM. It can be found that the agglomeration phenomenon and the transformation of NiO from block to strip are caused by the large volume expansion after 100 cycles (Fig. S3a, b). However, Fig. S3c, d shows that the integrity of the electrode is well preserved with no obvious change in morphology and structure for NiO@graphene after 100 cycles. From the SEM images, it confirms that the addition of graphene inhibits the volume expansion and aggregation of NiO to some extent. Figure 5c illustrates the unique 3D conductive network structure of NiO@graphene composite material and the NiO nanoparticles are well distributed on the graphene nanosheets. The reasons for the exceptional electrochemical properties of NiO@graphene can be explained as below. Firstly, the innovative 3D structure can provide more short pathways for ion/electron diffusion and large electrode/electrolyte contact area. Secondly, the network structure based on graphene nanosheets can enhance the structural stability of materials by relieving the aggregation and buffering the large volume expansion of the NiO nanoparticles. Furthermore, the graphene nanosheets with good electrical conductivity serve as conductive channels, leading to rapid charge transport. A comparison of the electrochemical properties of NiO@graphene with various reported NiO/C composites is presented in Fig. 5d [39, 55, 56, 60–64]. It is obvious shown that the NiO@graphene delivers a higher reversible capacity than other NiO/C composites, indicating NiO@graphene has a better rate capability.

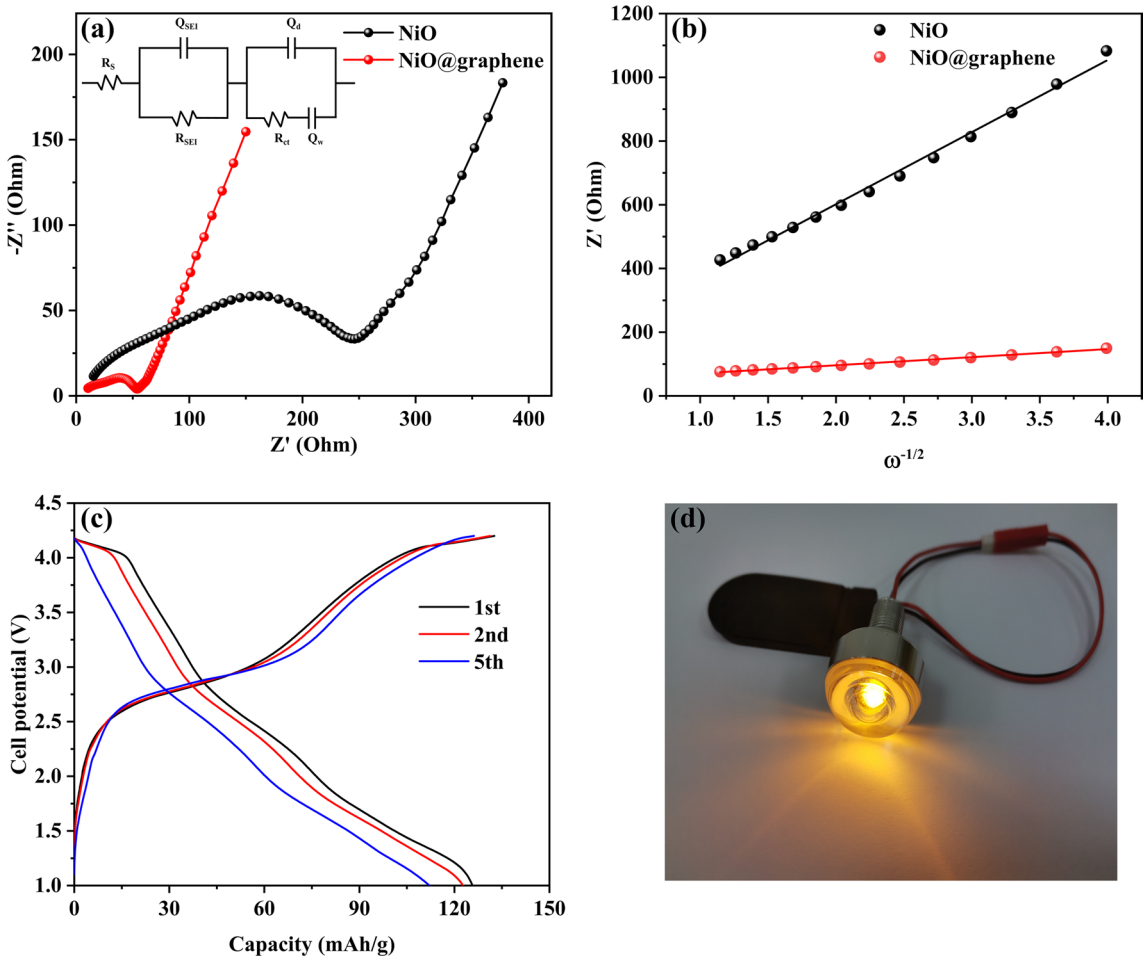

Fig. 6 Nyquist plots of two samples after 100 cycles (the inset is the equivalent circuit) **a**, relationship between Z'_{re} and $\omega^{-1/2}$ in the low-frequency region of the bare NiO and NiO@graphene samples **b**, charge/discharge curves for the full battery at 0.1 A g^{-1} **c**, the digital image for the practical application of the full cell **d**

To investigate the reaction kinetics of two electrodes, the electrochemical impedance spectroscopy (EIS) investigations were taken. Figure 6 depicts the Nyquist plots of two samples after 100 charge/discharge cycles (the inset was the equivalent circuit). Clearly, both samples possess two depressed semicircles in the high–medium-frequency region and an inclined line at low-frequency region. Generally, the intercept of the real impedance (Z') axis in the high frequency region is associated with internal resistance (R_S), which is considered as the resistance of electrolyte solution [12]. The first semicircle is assigned to the resistance for the migration of Li-ion through the SEI layer resistance (R_{SEI}), and the second semicircle was the charge transfer resistance (R_{ct}) at the interface of electrode/electrolyte, while the inclined line is related to the Warburg impedance (Q_W) describing Li-ion diffusion in the bulk electrode [65, 66]. Based on the above analysis, the detailed EIS fitting data are displayed in Table 1. Apparently, the diameters of the two

Table 1 Kinetic parameters obtained from the Nyquist plots for the samples

Samples	R_S (Ω^{-1})	R_{SEI} (Ω^{-1})	Q_{SEI}		R_{ct} (Ω^{-1})	Q_d		Q_W	
			Y_0 (Ω^{-1})	n		Y_0 (Ω^{-1})	n	Y_0 (Ω^{-1})	n
NiO	4.577	18.22	3.532×10^{-6}	0.8248	261.9	1.122×10^{-4}	0.4895	3.827×10^{-3}	0.6614
NiO@graphene	2.458	7.898	9.149×10^{-5}	0.9999	49.11	5.517×10^{-4}	0.3833	3.385×10^{-2}	0.6737

R_S—internal resistance, R_{SEI}—SEI resistance, Q_{SEI}—SEI capacitance, R_{ct}—charge transfer resistance, Q_d—interfacial capacitance, and Q_W—Warburg impedance

semicircles of NiO@graphene are smaller than that of NiO, reflecting that the NiO@graphene delivers a lower R_{ct} value (about 49 Ω)than that of NiO (about 262 Ω). This behavior may be induced by the conductive graphene that can alleviate volume expansion of NiO, thus facilitating the electron and Li^+ transfer during the repetitive cycling process with Li^+ intercalation and deintercalation reactions. The value of the constant phase angle element (CPE) is calculated by the following equation: $Q = {Y_0}^{-1} (j\omega)^{-n}$, where Y_0 is a constant independent of frequency, ω is the angular frequency, $j = (-1)^{1/2}$, and n is the exponential index [67]. According to the fitting data, the R_{SEI} value of NiO@graphene is about 8 Ω, which is lower than that of NiO (about 18 Ω). From this phenomenon, it can be inferred that graphene may greatly improve the stability of SEI structure and facilitate the lithium ions passing through the SEI film steadily, thus ensuring the favorable cycle performance of the NiO@graphene. Compared with NiO, the value of Q_W for NiO@graphene is much lower, which is beneficial to accelerate the mass transfer of charge in the Li-ion intercalation/deintercalation process and improve the lithium ions conductivity. As expected, the unique structure of NiO@graphene affords lower resistances, revealing a higher rate capability and cycling stability. Furthermore, Fig. 6b reveals the fitting result of the Warburg impedance coefficient (σ_w), which corresponds to Z' *vs* $\omega^{-1/2}$ slope. The Li-ion diffusion coefficient (${D_{Li}}^+$) can be evaluated from the following equations [47]:

$$Z'_{re} = R_s + R_{ct} + \sigma_w \omega^{-1/2}, \tag{1}$$

$$D^+_{Li} = R^2T^2/\left(2A^2n^4F^4C^+_{Li}2\sigma^2_w\right), \tag{2}$$

where R is gas constant, T means the absolute temperature (K), A represents the surface area of the electrode, n denotes the number of electrons transferred in the insertion process, F corresponds to Faraday constant, and ${C_{Li}}^+$ is the concentration of Li^+. The values of ${D_{Li}}^+$ are determined to be 1.82×10^{-14} and 1.44×10^{-12} cm^2 s^{-1} for bare NiO and NiO@graphene samples, respectively. Therefore, it can be elaborated that the introduction of the graphene contributes to the significant improvement in the kinetics of Li^+ diffusion. To further study its practical application, a full cell is constructed using the as-fabricated NiO@graphene electrode as anode and commercial $LiCoO_2$ material as the cathode. Figure 6c displays the 1st, 2nd and 5th of the full battery at 0.1 A g^{-1} in the range from 1.0 to 4.2 V. The full cell delivers the initial charge and discharge capacities being 132.6 mAh g^{-1} and 125.7 mAh g^{-1}, respectively, corresponding to an ICE of 94.8%. In addition, a yellow LED bulb is successfully lighted up by the as-prepared full battery (Fig. 6d), indicating its good application in our daily life.

Due to the superior rate capacity and excellent cycling performance of NiO@graphene electrodes, it is crucial to understand the contribution of two charge mechanisms: diffusion-dominated faradic process arising from Li^+ insertion/extraction and capacitive effect. As shown in Fig. 7a, CV tests of NiO@graphene with increasing scan rate from 0.1 to 1.0 mV s^{-1} were carried out. The power-law relationship between peak current (i) and sweep rate (v) can be expressed as follows [68, 69]:

$$i = av^b, \tag{3}$$

$$\log(i) = b\log(v) + \log(a), \tag{4}$$

in which a and b are adjustable parameters. Commonly, the value of b is close to 0.5 representing an ideal diffusion-dominated process, while b approaching 1 refers to a capacitive process. The b value can be obtained from the slope of the plots of $\log(i)$ *vs* $\log(v)$. Figure 7b exhibits the b values of 0.860, 0.713, 0.553, 0.604 and 0.611 at the anodic and cathodic peaks, indicating that surface-limited capacitive behavior plays a predominant part in Li-ion storage for NiO@graphene. Meanwhile, the corresponding capacitive contribution at a certain rate can be quantitatively calculated by separating the current response (i) into capacitive (k_1v) and diffusion-dominated ($k_2v^{1/2}$) reactions at a fixed potential (V), based on the Dunn's equation [70]:

$$i = k_1v + k_2v^{1/2}, \tag{5}$$

At a scan rate of 0.6 mV s^{-1} (Fig. 7c), the capacitive capacity contribution ratio of the NiO@graphene electrode makes up about 62% of the total current. Figure 7d and Fig. S4 demonstrate that the contribution ratio from capacitive capacity gradually rises with the increase in the scan rate (from 0.1 to 1.0 mV s^{-1}), especially, and attain a maximum value of 86.8% the capacitive capacity contribution at a scan rate of 1.0 mV s^{-1}. Meanwhile, the pure NiO electrode also presents a capacitive-controlled behavior (Fig. S5).

4 Conclusion

In this work, a facile and simple strategy is presented to prepare the NiO@graphene composite. The synergetic combination of graphene with high conductivity and the 3D structure is beneficial for the outstanding electrochemical properties for NiO@graphene composite. A large reversible capacity of 1366 mAh g^{-1} is attained for NiO@graphene at the current density of 0.05A g^{-1}. When it reached up to 10 A g^{-1}, NiO@graphene can show a reversible capacity of 711 mAh g^{-1}. Furthermore, NiO@graphene still displays a favorable reversible capacity of 205 mAh g^{-1} after 500th cycle at 0.05 A g^{-1}. In view of these results, NiO@graphene composites might provide promising anode candidates for high-rate LIBs.

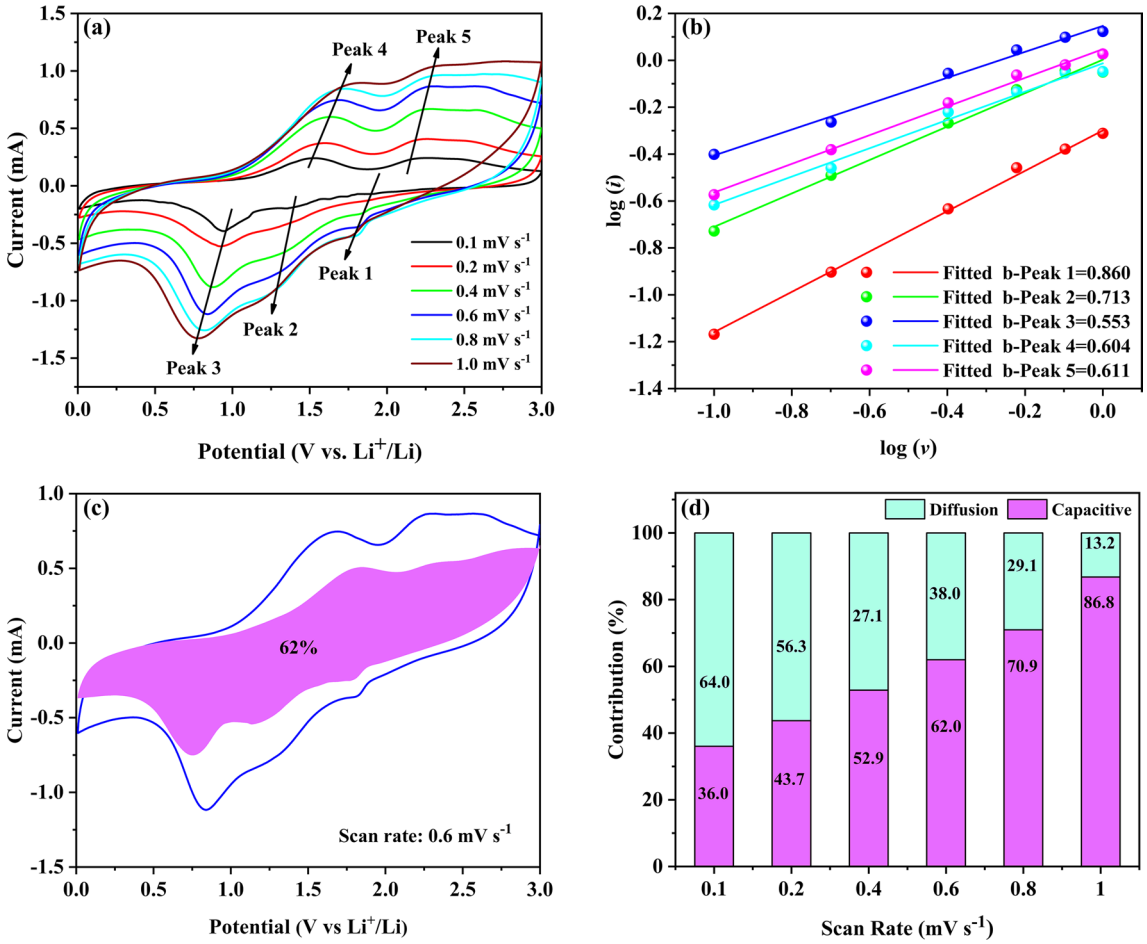

Fig. 7 Kinetic investigation of the electrochemical behavior of the NiO@graphene electrode *vs* Li^+/Li, CV profiles at various scan rates **a**, linear relationships between log(*i*) and log(*v*) **b**, separation of contributions from capacitance reaction at 0.6 mV s^{-1} **c**, capacitance and diffusion-controlled capacity to the total stored charge at various scan rates **d**

Supplementary Information The online version contains supplementary material available at https://doi.org/10.1007/s40195-021-01283-5.

Acknowledgements This work was supported by the Science & Technology Department of Sichuan Province (No. 2019YJ0665) and the Opening Project of Material Corrosion and Protection Key Laboratory of Sichuan Province (No. 2020CL10).

References

[1] X. Wang, L. Zhang, Z. Zhang, A. Yu, P. Wu, Phys. Chem. Chem. Phys. **18**, 3893 (2016)
[2] Z. Wang, Q. Gao, P. Lv, X. Li, X. Wang, B. Qu, J. Mater. Sci. Technol. **38**, 119 (2020)
[3] S. Qi, H. Wang, J. He, J. Liu, C. Cui, M. Wu, F. Li, Y. Feng, J. Ma, Sci. Bull. **66**, 685 (2021)
[4] X. Li, S. Qi, W. Zhang, Y. Feng, J. Ma, Rare Met. **39**, 1239 (2020)
[5] F. Li, J. He, J. Liu, M. Wu, Y. Hou, H. Wang, S. Qi, Q. Liu, J. Hu, J. Ma, Angew Chem. Int. Ed. Engl. **60**, 6600 (2021)
[6] R.C. Masse, C.F. Liu, Y.W. Li, L.Q. Mai, G.Z. Cao, Natl. Sci. Rev. **4**, 26 (2017)
[7] S. Mohapatra, S.V. Nair, A.K. Rai, Acta Metall. Sin. -Engl. Lett. **31**, 164 (2017)
[8] B. Ding, Z. Cai, Z. Ahsan, Y. Ma, S. Zhang, G. Song, C. Yuan, W. Yang, C. Wen, Acta Metall. Sin. -Engl. Lett. **34**, 291 (2020)
[9] L. Zhang, J. Yue, T. Wei, Z. Liu, J. Zhou, C. Liu, H. Jiang, Z. Jiang, Z. Fan, Carbon **142**, 327 (2019)
[10] X. Zhao, W. Jia, X. Wu, Y. Lv, J. Qiu, J. Guo, X. Wang, D. Jia, J. Yan, D. Wu, Carbon **156**, 445 (2020)
[11] W. Wang, X. Song, C. Gu, D. Liu, J. Liu, J. Huang, J. Alloys Compd. **741**, 223 (2018)
[12] J. Wu, W. Yin, W. Liu, P. Guo, G. Liu, X. Liu, D. Geng, W.M. Lau, H. Liu, L. Liu, J. Mater. Chem. A **4**, 10940 (2016)
[13] J. Liang, H. Hu, H. Park, C. Xiao, S. Ding, U. Paik, X. Lou, Energy Environ. Sci. **8**, 1707 (2015)
[14] Q. Li, Z. Yi, Y. Cheng, X. Wang, D. Yin, L. Wang, Appl. Surf. Sci. **427**, 354 (2018)
[15] H. Ren, Z. Wen, S. Chen, J. Liu, S.W. Joo, J. Huang, Mater. Chem. Phys. **232**, 229 (2019)
[16] G. Evmenenko, T.T. Fister, D.B. Buchholz, Q. Li, K.S. Chen, J. Wu, V.P. Dravid, M.C. Hersam, P. Fenter, M.J. Bedzyk, A.C.S. Appl, Mater. Interfaces **8**, 19979 (2016)
[17] X. Ruan, Y. Yang, K. Pu, M. Gao, Y. Liu, H. Pan, J. Power Sources **397**, 134 (2018)

[18] T.V. Thi, A.K. Rai, J. Gim, J. Kim, J. Power Sources **292**, 23 (2015)
[19] Q. Li, G. Huang, D. Yin, Y. Wu, L. Wang, Part. Part. Syst. Char. **33**, 764 (2016)
[20] J. Zhang, W. Luo, T. Xiong, R. Yu, P. Wu, J. Zhu, Y. Dai, L. Mai, Nanoscale **11**, 7588 (2019)
[21] Y. Zheng, Y. Li, J. Yao, Y. Huang, S. Xiao, Ceram. Int. **44**, 2568 (2018)
[22] G. Zhao, L. Zhang, C. Li, H. Huang, X. Sun, K. Sun, Chem. Eng. J. **328**, 844 (2017)
[23] Y. Feng, H. Zhang, W. Li, L. Fang, Y. Wang, J. Power Sources **301**, 78 (2016)
[24] L. Ouyang, Z. Cao, L. Li, H. Wang, J. Liu, D. Min, Y. Chen, F. Xiao, R. Tang, M. Zhu, Int. J. Hydrogen. Energ **39**, 12765 (2014)
[25] D. Wang, M. Gao, H. Pan, J. Wang, Y. Liu, J. Power Sources **256**, 190 (2014)
[26] L. Ouyang, Z. Cao, H. Wang, R. Hu, M. Zhu, J. Alloys Compd. **691**, 422 (2017)
[27] T. Liu, C. Jiang, B. Cheng, W. You, J. Yu, J. Power Sources **359**, 371 (2017)
[28] J. Tian, Q. Shao, X. Dong, J. Zheng, D. Pan, X. Zhang, H. Cao, L. Hao, J. Liu, X. Mai, Z. Guo, Electrochim. Acta **261**, 236 (2018)
[29] G. Li, Y. Li, J. Chen, P. Zhao, D. Li, Y. Dong, L. Zhang, Electrochim. Acta **245**, 941 (2017)
[30] Y. Gong, M. Zhang, G. Cao, RSC Adv. **5**, 26521 (2015)
[31] K.S. Novoselov, A.K. Geim, S.V. Morozov, D. Jiang, Y. Zhang, S.V. Dubonos, I.V. Grigorieva, A.A. Firsov, Science **306**, 666 (2004)
[32] L. Gao, C. Gu, H. Ren, X. Song, J. Huang, Electrochim. Acta **290**, 72 (2018)
[33] X. Cai, L. Lai, Z. Shen, J. Lin, J. Mater. Chem. A **5**, 15423 (2017)
[34] C. Lin, L. Yang, L. Ouyang, J. Liu, H. Wang, M. Zhu, J. Alloys Compd. **728**, 578 (2017)
[35] C. Lin, L. Ouyang, C. Zhou, R. Hu, L. Yang, X. Yang, H. Shao, M. Zhu, J. Power Sources **443**, 227276 (2019)
[36] H. Fang, L. Zhao, W. Yue, Y. Wang, Y. Jiang, Y. Zhang, Electrochim. Acta **186**, 397 (2015)
[37] J. Yan, L. Kong, Y. Ji, J. White, Y. Li, J. Zhang, P. An, S. Liu, S.T. Lee, T. Ma, Nat. Commun. **10**, 1 (2019)
[38] T. Zhu, X. Li, Y. Zhang, M. Yuan, Z. Sun, S. Ma, H. Li, G. Sun, J. Electroanal. Chem. **823**, 73 (2018)
[39] Z. Zhang, X. Zhang, X. You, M. Zhang, M.D. Walle, J. Wang, Y. Li, Y. Liu, J. Nanopart. Res. **18**, 247 (2016)
[40] M.L. Huang, C.D. Gu, X. Ge, X.L. Wang, J.P. Tu, J. Power Sources **259**, 98 (2014)
[41] F. Liu, X. Wang, J. Hao, S. Han, J. Lian, Q. Jiang, Sci. Rep. **7**, 17709 (2017)
[42] X. Xu, H. Tan, K. Xi, S. Ding, D. Yu, S. Cheng, G. Yang, X. Peng, A. Fakeeh, R.V. Kumar, Carbon **84**, 491 (2015)
[43] X. Meng, J. Zhu, H. Bi, Y. Fu, Q. Han, X. Wang, J. Mater. Chem. A **3**, 21682 (2015)
[44] H. Kahimbi, S. Hong, M. Yang, B.G. Choi, J. Electroanal. Chem. **786**, 14 (2017)
[45] A. Roy, A. Ray, S. Saha, M. Ghosh, T. Das, B. Satpati, M. Nandi, S. Das, Electrochim. Acta **283**, 327 (2018)
[46] J. Shao, H. Zhou, J. Feng, M. Zhu, A. Yuan, J. Alloys Compd. **784**, 869 (2019)
[47] W. Jae, J. Song, J. Hong, J. Kim, J. Alloys Compd. **805**, 957 (2019)
[48] I. Elizabeth, A.K. Nair, B.P. Singh, S. Gopukumar, Electrochim. Acta **230**, 98 (2017)
[49] J. Chen, X. Wu, Q. Tan, Y. Chen, New J. Chem. **42**, 9901 (2018)
[50] Y. Xia, B. Sun, S. Zhu, S. Mao, X. Li, B. Guo, Y. Zeng, H. Wang, Y. Zhao, J. Solid State Chem. **269**, 132 (2019)
[51] C. Wang, Y. Zhao, D. Su, C. Ding, L. Wang, D. Yan, J. Li, H. Jin, Electrochim. Acta **231**, 272 (2017)
[52] X. Huang, P. Zhang, J. Wu, Y. Lin, R. Guo, Mater. Lett. **153**, 102 (2015)
[53] C. Chen, P.J. Perdomo, M. Fernandez, A. Barbeito, C. Wang, J. Energy Storage **8**, 198 (2016)
[54] S.G. Hwang, G.O. Kim, S.R. Yun, K.S. Ryu, Electrochim. Acta **78**, 406 (2012)
[55] C. Ding, W. Zhou, X. Wang, B. Shi, D. Wang, P. Zhou, G. Wen, Chem. Eng. J. **332**, 479 (2018)
[56] Y. Xu, S. Hou, G. Yang, T. Lu, L. Pan, J. Solid State Electr. **22**, 785 (2017)
[57] P. Xiong, J. Zhu, L. Zhang, X. Wang, Nanoscale Horiz **1**, 340 (2016)
[58] Q. Li, C. Feng, Z. Guo, Ceram. Int. **42**, 7888 (2016)
[59] X. Zhu, J. Hu, H. Dai, L. Ding, L. Jiang, Electrochim. Acta **64**, 23 (2012)
[60] W. Shi, Y. Zhang, J. Key, P. Shen, J. Power Sources **379**, 362 (2018)
[61] X. Li, L. Fan, X. Li, H. Shan, C. Chen, B. Yan, D. Xiong, Mater. Chem. Phys. **217**, 547 (2018)
[62] K. Han, Y. Zhang, N. Zhang, G. Li, J. Wang, G. Xie, L. Zhang, J. Nanosci. Nanotechnol. **20**, 2514 (2020)
[63] X. Zhang, Q. Huang, M. Zhang, M. Li, J. Hu, G. Yuan, J. Alloys Compd. **822**, 153718 (2020)
[64] Z. Fan, J. Liang, W. Yu, S. Ding, S. Cheng, G. Yang, Y. Wang, Y. Xia, K. Xi, R.V. Kumarb, Nano Energy **16**, 152 (2015)
[65] X. Zhou, F. Chen, T. Bai, B. Long, Q. Liao, Y. Ren, J. Yang, Green Chem. **18**, 2078 (2016)
[66] M. Jiang, M. Jiang, H. Gao, J. Chen, W. Liu, Y. Ma, W. Luo, J. Yang, Acta Metall. Sin. -Engl. Lett. **34**, 337 (2020)
[67] L. Chen, Y. Zhang, C. Lin, W. Yang, Y. Meng, Y. Guo, M. Li, D. Xiao, J. Mater. Chem. A **2**, 9684 (2014)
[68] Y. Fu, L. Li, S. Ye, P. Yang, P. Liao, X. Ren, C. He, Q. Zhang, J. Liu, J. Mater. Chem. A **1**, 453 (2021)
[69] X. Yang, Y. Wang, B. Hou, H. Liang, X. Zhao, H. Fan, G. Wang, X. Wu, Acta Metall. Sin. -Engl. Lett. **34**, 390 (2020)
[70] J. Wang, J. Polleux, J. Lim, B. Dunn. J. Phys. Chem. C **111**, 14925 (2007)